Evidence for excess argon during high pressure metamorphism in the Dora Maira Massif (Western Alps, Italy), using an ultra-violet laser ablation microprobe (super 40) Ar- (super 39) Ar technique

Nicolas Arnaud, Simon P Kelley

Evidence for Excess Argon during High Pressure Metamorphism in the Dora Maira Massif (Western Alps, Italy), using an Ultra-Violet Laser Ablation Microprobe ^{40}Ar-^{39}Ar technique.

N.O. ARNAUD* and S.P. KELLEY

Dpt. of Earth Sciences, Open University, Milton Keynes, UK

* now at URA 10, Dpt des Sci. de la Terre, Clermont-Ferrand, FR

Abstract

Ultra-high pressure eclogite/amphibolite grade metamorphism of the Dora Maira Massif in the western Alps is a well established and intensively studied event. However, the age of peak metamorphism and early cooling remains controversial. ^{40}Ar-^{39}Ar step-heating ^{40}Ar-^{39}Ar and laser spot ages from high pressure phengites yield plateau ages as old as 110Ma which have been interpreted as the time of early cooling after the high pressure event. Recent U/Pb and Sm/Nd results challenge this assertion, indicating a much younger age for the event, around 45 Ma, and hence a radically different timing for the tectonic evolution of the western Alps. In a new approach to the problem, samples from the undeformed Hercynian metagranite, Brossasco, were studied using an ultra-violet laser ablation microprobe technique for ^{40}Ar-^{39}Ar dating. The new technique allowed selective in situ analysis, at a spatial resolution of 50 µm, of quartz, phengite, biotite and K-feldspar. The results demonstrate the frequent occurence of excess argon with high $^{40}Ar/^{36}Ar$ ratios (1000-10000) and a strong relationship between apparent ages and metamorphic textures. The highest excess argon ratios are always associated with high closure temperature minerals or large diffusion domains within single mineral phases. The best interpretation of this relationship seems to be that excess argon was incorporated in all phases during the high pressure event, then mixed with an atmospheric component during rapid cooling and retrogression, producing a wide range of argon concentrations and $^{40}Ar/^{36}Ar$ ratios. Step-heating analsysis of minerals with this mixture would produce linear arrays on a $^{36}Ar/^{40}Ar$ vs $^{39}Ar/^{40}Ar$

correlation diagram, leading to geologically meaningless plateau ages, older than the true closure age. In the present case, some ages in the range 60-110 Ma could be explained by the presence of excess argon incorporated around 40-50 Ma ago. Similar results found in other high-pressure terrains in the Alps may reconcile the argon geochronometer with other systems such as Rb/Sr, U/Pb or Sm/Nd. This study therefore calls for an increasing use of high resolution in-situ sampling techniques to clarify the meaning of $^{40}Ar/^{39}Ar$ ages in many high pressure terrains.

Introduction.

The Alps, with the Himalayan system, have been historically important in furthering understanding of continental collision. Understanding the geodynamic evolution of the alpine collision is therefore an important step in the study of continental tectonics and to achieve that aim we must understand not only the mechanisms but also the rates of the processes involved. The discovery of coesite-bearing ultra-high pressure rocks in the western alps (Chopin, 1984) was an important advance in the understanding of the subduction-related processes and assessing the age of this high pressure (HP) event is essential since its timing defines the collision age as well as the post-collision cooling history.

The age of the HP metamorphism is still controversial. While some U/Pb and ^{40}Ar-^{39}Ar ages have suggested an eo-alpine high pressure phase ranging from 90 Ma to 120 Ma (Paquette et al. 1989, Monié and Chopin, 1991; Scaillet et al., 1990; Scaillet et al., 1992) partially reset by a later eocene-oligocene greenschist phase (Chopin and Maluski, 1980; Monié, 1985), recent Sm/Nd, U/Pb and Rb/Sr work (Tilton et al. 1989, 1991, Bowtell et al., 1994) has strongly suggested a very different scenario in which the age of the HP event is ca. 40-50 Ma, casting doubt upon the existence of an eo-alpine event and upon the interpretation of the late greenschist overprint.

^{40}Ar-^{39}Ar dates on phengite by a variety of techniques have produced ages from 40 Ma to as old as 130 Ma with a cluster in the range 60-90 Ma. It has also been suggested (Monié and Chopin, 1991; Scaillet et al., 1992) that high pressure phengite could preserve ^{40}Ar-^{39}Ar ages older than equivalent Rb/Sr, implying unusually high blocking temperatures for argon diffusion in this mineral. Although sometimes reported for high grade metamorphic terrains (Maluski et al., 1990), the influence of excess

argon has rarely been documented in such an ultra-HP environment, (Li et al., 1994) while its effect is of prime importance (Vidal and Hunziker, 1985). To study this question and its possible consequences on ^{40}Ar-^{39}Ar ages, we selected a sample with a variety of mineral phases, the Brossasco metagranite in the Dora Maira massif, which has seen the HP event without being extensively affected by the later greenschist facies overprint. The new ultra-violet laser ablation microprobe (UVLAMP) allowed us to quantitatively study the relationship of apparent ages of a variety of mineral, including feldspars and quartz to metamorphic microtextures. The results yield important information on the evolution of excess argon in metamorphic fluids.

Geological Setting and Sample Description.

The Dora Maira massif (Vialon, 1966) lies in the internal part of the western Alps (Fig.1) and contains continental eclogitic rocks thought to have been subducted in excess of 150 km in depth (Chopin, 1984, Chopin et al., 1991) under an oceanic complex now forming the overlying Piemonte nappe. The Brossasco metagranite belongs to the Brossasco-Isasca complex (Biino et al, 1988, and fig.1), a little deformed tectonic unit metamorphosed at ultra-high pressure (Chopin et al., 1991; Biino and Compagnoni, 1992: Henry et al., 1993). The protolith is an Hercynian granite of poorly known age, though a U/Pb age on zircon suggests an age of 303Ma (Paquette, personnal communication in Henry et al. 1993) which compares well with the ages in the range ^{38}0-304 Ma obtained on gneisses at Parigi, a few kilometres to the north (Tilton et al., 1991). The main mineral phases of the protolith were probably Quartz(Qz) + K-feldspar(Kfd) + Biotite (Bio). Though the igneous texture is still remarkably fresh, only K-feldspars remain from the igneous mineralogy, which is now replaced by a polymetamorphic assemblage characteristic of the eclogitic metamorphism and the amphibolite retrogressive facies with Phengite(Ph) + Bio + Kfd + Albite(Ab) + Qz + Jadeite(Jd) + Garnet(Gt) + Rutile(Rt). A complete review of the metamorphic textures and reactions is given in Biino and Compagnoni (1992). In some samples dated during this study, an early assemblage of Ph and Gt appears largely destabilized and surrounded by two reaction coronae: a first one of red Bio (Bio1), and a second one of minute Bio and Qz (not analysed here). This external rim is in turn surrounded by granoblastic euhedral monocristalline Qz grains, thought to be pseudomorphs after coesite (Biino and Compagnoni, 1992). Large igneous Kfds

(Kfd1) are cut by small bands of granoblastic Ab + Kfds(Kfd2) (<50 μm) grains, and Bio bands (Bio2). The Ab+Kfd2 bands may be related to a weak and late greenschist overprint though there is no association with late stage structures such as shears. Moreover only little evidence of greenschist retrogression was reported by Biino and Compagnoni (1992).

Analytical Procedures.

Two samples were prepared as thick sections (100-150m thick), polished on one side, and irradiated at the Ford Reactor, Michigan. Previous work with a similar techniques (Kelley et al., 1994) showed that no artefacts (such as cracks or contamination) are introduced by this preparation technique. J values were calculated using the hornblende standard, Mmhb1 (520.4Ma). After irradiation, samples were loaded into a standard laser port with a sapphire window which has a high transmission coefficient for light at 266nm. An additional sapphire window, 1mm thick, was placed between the laser port window and the samples to prevent ablated material coating the laser port window. A Spectron Laser Systems SL401 with two temperature and angle controlled KD*P crystals was used as the UV laser source. The laser produces pulsed light with a wavelength of 1064nm (IR) which is frequency-doubled by the first KD*P crystal to a wavelength of 532nm and then doubled again by the second crystal to a wavelength of 266nm (UV). The wavelengths were separated using a Pellin Brocca prism, and the resulting ultra-violet laser pulses have energies of up to 20mJ per pulse, and a pulse length of 10ns at a repetition rate of 10Hz. The beam was directed using high reflectance, oxide coated mirrors, into a customised Leica Metallux 3 microscope. Inside the microscope, the beam was re-directed through an ultra-violet refracting objective lens, and focused to a spot size of less than 10μm at the sample surface. The effects of UV laser ablation upon natural silicates differs from infra-red and visible lasers (Kelley et al., 1994), in that argon is released from very small volumes during each laser pulse, allowing close control of the extraction process. In the present study, the laser was repeatedly rastered across areas from 50μm^2 to 100μm^2, producing square and rectangular ablation pits with depths up to that of the section (Fig. 2) in a matter of 1-7 minutes. Despite the extended laser ablation times, negligible argon is extracted from beyond the visible margins of the pits, even in quartz (Kelley et al., 1994), allowing direct correlation of in situ argon isotope analyses with metamorphic textures. Microprobe analyses have been

carried out after lasering in order to chemically characterize the different metamorphic phases (Table 1) and also to analyse the phases adjacent to the location as the laser ablation pits.

Results .

Analyses of quartz grains (Table 2) from the granoblastic texture (after coesite) contained variable quantities of excess argon and gave impossibly high ages from a few 100's of Ma to near infinity. It is clear from microprobe data that during the amphibolite facies retrogression, Bio1 grew at the expense of Ph leading to complex intergrown textures below the spatial resolution of the laser beam (fig. 3a). It apparently also affects the microprobe data as can be seen on table 1, where analysis never reach a purely phengitic composition. The same is true for Bio1. Cores of Ph optically free of Bio1 yielded ages of 565 and 614 Ma. Given the presence of excess argon in the quartz, and U/Pb analyses indicating Hercynian ages for intrusion, we conclude that early phengites contain high concentrations of an excess argon component with high and variable $^{40}Ar/^{36}Ar$ ratios. The retrogression coronae (Bio1) adjacent to the early phengites yield ages ranging from 228 Ma down to 156 Ma, while the mixed zones of Ph+Bio1 are in the range 355 Ma to 484 Ma, as expected. Note that even the youngest ages of Bio1 are well above the inferred age of the UHP peak metamorphism as inferred by U/Pb (Tilton et al., 1991). No correlation between ^{39}Ar contents and age, nor significant Qz content, were seen in Bio1 suggesting that high apparent ages were not the result of occluded Qz possibly fused or heated during the analysis of biotites. Moreover, biotites in shear bands outside the coronae yielded ages in the range 32 Ma to 86 Ma, similar to ages from other phengites and biotites already reported in the literature. Large igneous K-feldspars yielded ages generally in the range 25Ma to around 42Ma with a spread up to 83Ma. Note that the large igneous feldspars generally yield the youngest ages measured. In contrast, small granoblastic grains of Kfd2+Ab in deformed zones within the igneous feldspars, yield older ages in the range 107 Ma to 626 Ma. A UVLAMP traverse across a boundary between original igneous K-feldspar (Kfd1) and recrystallised Kfd2 + Ab revealed the sharp contrast which corresponds precisely with the boundary (Fig 3b). Many ages from the granoblastic bands exceed the original intrusion age for the granite and clearly reflect the incorporation of excess argon. This contrast is also clear in the microprobe traverse showing contrasting Or contents (from Or95Ab5 to Or5Ab95) between the two generations of feldspars.

The ^{39}Ar released by rastering similar sized pits in minerals using the UV laser vary by around 10 to 20%. Larger variations in some of the analyses reported here are probably due to cratering (which is particularly evident in fine grained quartz), fluid inclusions, and intergrowth of minerals below the surface of the section.

Interpretation of the age ranges.

It is clear that some of the apparent ages, particularly from phengite and K-feldspar reflect the incorporation of excess argon with high $^{40}Ar/^{36}Ar$ ratios. Graphical representation of such data generally takes the form of a correlation diagram, a plot of $^{36}Ar/^{40}Ar$ versus $^{39}Ar/^{40}Ar$ (eg. Roddick et al., 1973; Heizler and Harrison, 1988). On such a diagram, some systems plot as a simple binary mixing line, in which the intercept of the line with the abscissa gives the $^{39}Ar/^{40}Ar$ ratio, hence the age of the sample. The intercept of the line with the ordinate axis often corresponds with the modern atmospheric $^{40}Ar/^{36}Ar$ ratio (295.5). However a good fit to the data can be achieved only when the isotopic composition of the contaminant is homogeneous and the proportions of the three reference isotopes vary in different fractions of gas. A weakness of the technique is thus that it is often difficult to assess the presence of extraneous argon (inherited or later incorporated), in laser spot or step heating analyses, when the data are clustered close to the $^{39}Ar/^{40}Ar$ axis. A more complex situation arises when the extraneous component is inhomogeneous, and the data tend to fall in triangular envelope defined by the $^{39}Ar/^{40}Ar$ ratio for the age, and a range of $^{36}Ar/^{40}Ar$ ratios representing the end members of the inhomogeneous contaminant.

When plotted on a correlation diagram (fig. 4) the Brossasco data points define a broad triangular envelope, spreading from the excess-Ar rich Ph, Qz and Kfd2 through Bio1 with a range of excess concentrations to the youngest ages which were obtained from Bio2 and Kfd1. The youngest ages fall close to ages obtained by other geochronological techniques or by ^{40}Ar-^{39}Ar on rocks affected by greenschist retrogression or even some on HP phengites lacking pervasive alteration or retrogression. The broad trend suggests mixing between several end-members: an excess component with a very high

$^{40}Ar/^{36}Ar$ ratio (in excess of 10000), a component with an argon isotope ratio near atmospheric (295.5), and at least one radiogenic component (age). Preservation of the highest excess argon concentrations in phases with the highest closure temperatures (or possibly the largest diffusion domains for K-feldspars) which are also the phases most associated with the high pressure metamorphism (Ph, Qz after coesite, and possibly recrystallized Kfd2) implies that the high pressure event was associated with fluids rich in argon with a $^{40}Ar/^{36}Ar$ ratio of at least 10000. Association of the retrogressive phase (Bio1) and unrecrystallised K-feldspar which have lower closure temperatures with lower concentrations of excess argon with very variable and lower $^{40}Ar/^{36}Ar$ ratios suggest three possible scenarios.

1- Incorporation of a large quantity of excess argon during UHP peak metamorphism, followed by a partial redistribution of argon during retrogression;

2- Incorporation of argon during the UHP peak, but also during the retrogression path. This in turn implies a decreasing $^{40}Ar/^{36}Ar$ in the excess argon during retrogression (increasing influence of fluid with an 'atmosphere-like' isotopic composition);

3- Progressive incorporation of excess argon from a finite reservoir (for example the grain boundary network) in closed system, with decreasing partial pressure of argon as a result of incorporation in minerals.

Given the apparent diversity of $^{40}Ar/^{36}Ar$ initial ratios in the different minerals, and the fact that most K-bearing minerals exhibit lower $^{40}Ar/^{36}Ar$ ratios than Qz (which is most probably dominated by the actual fluid in inclusions), the first two scenarios are more likely. The main difference between (1) and (2), is that the system may behave either as a closed system at a scale above that of individual minerals (1) or as an open system (2). Unfortunately it is not possible to distinguish between the two using the present data. In either scenario, the wide range of excess argon concentrations and ratios implies that the mixing and re-equilibration of the minerals never reached completion. Sources of excess argon with high $^{40}Ar/^{36}Ar$ may have included: old deep crustal rocks, upper mantle, or simply the Brossasco metagranite itself. Biino and Compagnoni (1992) suggest that the granite may have been dry, precluding a pervasive effect of the greenschist overprint. Such a scenario would also preclude argon mobility during UHP metamorphism, allowing for only local redistribution of argon , producing variable concentrations of excess argon depending upon fluid inclusion concentrations and partition coefficients.

It seems likely therefore that incorporation of the high (circa 10000) $^{40}Ar/^{36}Ar$ component occurred during or soon after the HP metamorphism (now preserved in HP phases such as Ph) while redistribution and/or mixing with an atmospheric component occurred during retrogression following the HP event. The redistribution may have occurred during breakdown of the early HP phases and release of the excess argon rich end-member, which was variably reincorporated and mixed with a progressively decreasing lower $^{40}Ar/^{36}Ar$ component during recrystallization. In order for this pattern to have been preserved, the retrogression must have been accompanied by extremely rapid cooling such that many of the minerals passed through their closure temperatures before the excess argon component either equilibrated or was lost from the system. Note that retrogression from Ph to Bio in the coronae occurred at around 11kbar-575°C (Schertl et al., 1991), some 275°C above the closure temperature of biotite. The existence of age discrepancies in many other radiometric systems such as Sm/Nd or U/Pb suggests that isotopic equilibrium was not achieved prior to closure of the various systems. Given the relatively low diffusivity of those species (Sm, Nd, U, Pb...), redistribution of these elements must have taken place while metamorphic reactions were still active, during recrystallisation.

The K-feldspars seem to exhibit the presence of microstructures with varying argon retentivities, behaving as more or less separate reservoirs (Fig 3b). This micro-structure is also reflected in associated stepped heating studies (which will be discussed elsewhere) which yield patterns similar to those of Foster et al. (1990). Thus the range of ages from individual Kfd grains reflects the evolution of argon components in the rock since peak metamorphism during progressive closure of the different micro-structures in Kfd. Small Kfd grains (Kfd2), crystallized at the beginning of the retrogressive path when the partial pressure of excess Ar was high and retained anomalously high apparent ages as they closed prior to much of the mixing. Large plates of igneous K-feldspar (Kfd1), having suffered the HP peak deformation/metamorphism and not recrystallised, had smaller diffusion domains or higher defect densities and were less retentive to Ar. Ages from the large unrecrystallised plates therefore reflect later closure to argon diffusion as the influence of excess argon was waning.

Consequences of the mixing hypothesis.

One of the implications of incorporation of excess argon during the UHP peak metamorphism is the production of apparent trends in the clustered data on the correlation diagram. A simple model can be

used to illustrate this effect (Fig. 5), using a range of $^{39}Ar/^{40}Ar$ and $^{36}Ar/^{40}Ar$ ratios chosen to represent partially re-equilibrated minerals such as those in the Brossasco metagranite. The initial envelope in figure 5, represents the area in which the data might be expected to cluster prior to radiogenic argon accumulation. Subsequent envelopes represent the position and shape of the cluster after various lengths of time, assuming a closed system bahaviour from the time of excess incorporation. Most initial envelopes, even those with highly variable initial ratios, yield sub-linear trends with negative slopes after some millions of years. Moreover, lines fitted to the trends intercept increasingly close to the atmospheric ratio and the goodness of fit improves with time. It seems therefore that mixing followed by radiogenic production can lead to spurious linear trends almost indistinguishable from simple binary mixing, yielding well defined but geologically meaningless ages. Step-heating, which tends to emphasise edge to centre variations (variations in the $^{36}Ar/^{40}Ar$ ratios in this case), but averages differences between concentrations in grains of the same size or which outgas at the same temperature (variations in the $^{39}Ar/^{40}Ar$ ratios), will tend to enhance the spurious trends when applied to pure mineral separates, resulting in data in which it is difficult to find clear evidence for the presence of excess argon. Laser spot fusion of single separated minerals containing excess argon also leads to a scatter in ages which is difficult to assess. In the Brossasco case, the very high $^{40}Ar/^{36}Ar$ ratios mean that data points cluster in the lower part of the correlation diagram, away from the ordinate. In cases where the concentration and $^{40}Ar/^{36}Ar$ ratio are relatively constant, they may be tied by low temperature data closer to the ordinate reflecting contamination with modern atmospheric argon during analysis. Anomalously high step-heating plateaus, such as those seen in phengite from Dabie Shan (Li et al, 1994), may be the result.

Although many ^{40}Ar-^{39}Ar plateaus on the alpine HP phengites are certainly true ages, it is interesting to note that the inverse isochrons through data from some of the older ages in the literature fit the types of trends our modelled mixtures predict will occur after 40 Ma of time integrated growth. Moreover, because the data are clustered, and because the regressions are often directed by a few low-temperature points with high atmospheric Ar content, it is impossible to distinguish artefacts from geological reality in such trends. The common, concave-down age spectra, may also be interpreted along the same lines. Usually attributed to variable resetting of plateau ages or mixture of grain populations with different ages, these might be the result of falling isotopic ratios during cooling or recrystallisation. The lowest $^{40}Ar/^{36}Ar$ ratios which are related to the younger apparent ages ages, may have been

incorporated in the less retentive sites or sites closely associated with early dehydroxylation during step-heating. This signature will therefore be released early during step heating producing apparently partially reset plateaus.

Scaillet et al. (1992) ruled out the presence of excess argon to explain old phengite ages they found using laser spot analyses, on the basis that garnets in their samples did not show large quantities of excess argon. However, it is clear in our data that Qz incorporated argon with extreme $^{40}Ar/^{36}Ar$ ratios only in small quantities. The concentration of excess argon is much higher in the Ph than in the Qz, implying a high partition coefficient for argon between Ph and Qz. Similarly, argon may not be incorporated preferentially in garnets and would therefore be difficult to detect.

Implications for the ^{40}Ar-^{39}Ar age of the HP phase in the western Alps.

It is likely that the distribution of excess argon in our samples was controlled by two factors: 1) metamorphic textures produced at or just after peak metamorphism (the partial recrystallisation of feldspar and partial retrogression of phengite), 2) rapid closure of several mineral systems (Ph, Bio and Kfd) during mixing between excess rich and excess poor fluids. Moreover, 40 to 50 Ma of radiogenic production following the UHP peak metamorphism are sufficient to produce slightly scattered linear trends indicating apparent ages of 60 to 110 Ma, depending on the initial $^{40}Ar/^{36}Ar$ ratios.

The lack of isotopic equilibrium between three mineral systems (Ph, Bio, Kfd) indicates very rapid cooling, an observation which concurs with the studies of mineral equilibria in related areas (Schertl et al., 1991; Lardeaux and Spalla, 1991) and fisson track studies (Hurford et al., 1991), Sm/Nd and U/Pb results suggesting ages in the range 40 to 45 Ma for the HP peak metamorphism and estimates for the age of blueschist facies metamorphism in adjacent units such as the overlying Dronero-Sampeyre (Monié and Philippot, 1989; Goffé and Chopin, 1986).

The present data cannot uniquivocally rule out the existence of an eo-alpine HP event (cf. Vialette and Vialon 1964, Hunziker 1989). Such an event has been indicated in the eastern Alps (Thoni and Jagoutz, 1993). However, the presence of excess argon in samples from Dora Maira (Kelley et al., 1994) indicates that ^{40}Ar-^{39}Ar ages in the range 110 Ma to 50 Ma should be regarded with great care.

Conclusions.

In the Brossasco metagranite, minerals hthat suffered the HP conditions or hwhich recrystallized during the amphibolite grade retrogression show ages ranging from 40 Ma to 614 Ma, in a granite with U-Pb age of ca. 300 Ma. Excess argon with varying isotopic ratios has been measured using a new high resolution ultra-violet laser ablation microprobe, in phengite, biotite, quartz and K-feldspar. Though the existence of the eo-alpine HP event in the Western Alps cannot be dismissed by our data, old ^{40}Ar-^{39}Ar ages may be reconciled with recent Sm/Nd and U/Pb ages which suggest that the peak metamorphism is 40-45 Ma old. The old argon ages are the result of artefacts caused by incorporation of variable excess argon, with $^{40}Ar/^{36}Ar$ ratios up to 10000, followed, during retrogression, either by redistribution of that excess or incorporation of a lower $^{40}Ar/^{36}Ar$ component.

This result may explain the apparent paradox that phengite ^{40}Ar-^{39}Ar ages are often older than Rb/Sr ages not only in the Alps but also in other orogens (Schermer et al., 1990 for example, Li et al., 1994). Experimental assesment of the real closure temperature of phengite is urgently required. We suggest that the phengite closure temperatures need not be as high as previously suggested from comparison with Rb/Sr data. Incorporation of excess argon with high $^{40}Ar/^{36}Ar$ ratios during high pressure metamorphism may be a frequent phenomenon affecting phengite and other associated minerals, even in older orogens, causing them to yield higher ^{40}Ar-^{39}Ar than other associated geochronometers.

Finally, the UVLAMP system provides a new and powerful way to analyse fine metamorphic textures and as such could become invaluable in many geochronological studies.

Aknowledgments:

P. Monié, H. Maluski and J. Wheeler are greatly thanked for providing the samples. Thourough reviews by Ch. Chopin, H. Maluski, Ph. Monié and an anonymous reviewer greatly helped to clarify the paper. N. Arnaud was supported by an EEC fellowship during his stay at the Open University.

References.

Biino G, Compagnoni R, Lombardo B, Sandrone, R (1988) The pyrope-coesite-phengite-kyanite-talc whiteschist of case Parigi, southern Dora Maira massif. In: High pressure eclogitic reequilibration in the western Alps, Piccardo ed, IGCP N°235, Genova

Biino GG, Compagnoni R (1992) Very-high pressure metamorphism of the Brossasco coronite metagranite, southern Dora Maira massif, Western Alps. Schweiz Miner Petrogr Mitt 72: 347-363

Bowtell SA, Cliff RA, Barnicoat AC (1994) Sm-Nd isotopic evidence on the age of eclogitization in the Zermatt-Saas ophiolite. J Metamorphic Geol 12: 187-196

Chopin C, Maluski H (1980) $^{40}Ar/^{39}Ar$ dating of high pressure metamorphic micas from the gran Paradiso ares (Western Alps). evidence against the blocking temperature concept. Contrib Mineral Petrol 74: 109-122

Chopin C (1984) Coesite and pure pyrope in high grade blueschists of the Western Alps. a first record and some consequences. Contrib Miner Petrol 86: 107-118

Chopin C, Henry C, Michard A (1991) Geology and petrology of the coesite-bearing terrain, Dora Maira massif. Western Alps Eur J Mineral 3: 263-291

Foster DA, Harrison TM, Copeland P, Heizler MT (1990) Effects of excess argon within large diffusion domains on K-feldspar age spectra. Geochem Cosmochim Acta 54: 1699-1708

Goffé B, Chopin C (1986) High pressure metamorphism in the western Alps, zoneography of metapelites, chronology and consequences. Schweiz Miner Petrogr Mitt 66: 41-52

Henry C, Michard A, Chopin C (1993) Geometry and structural evolution of ultra-high-pressure and high-pressure rocks from the Dora Maira massif. Western Alps, Italy. J of Struc Geol 15, vol 8: 965-981

Heizler MT, Harrison TM (1988) Multiple trapped argon isotope components revealed by $^{40}Ar/^{39}Ar$ isochron analysis. Geochem Cosmochim Acta 52: 1295-1303

Hunziker JC, Desmons J, and Martinotti G (1989) Alpine thermal evolution in the Central and Western Alps. In Alpine Tectonics, Coward and Park ed, Spec Publs Geol Soc Lond 45: 353-367

Hurford AJ, Hunziker JC, Stöckhert B (1991) Constraints on the late thermotectonic evolution of the Western Alps. evidence for episodic rapid uplift. Tectonics 10, N°4: 758-769

Lardeaux JM, Spalla MI (1991) From granulites to eclogites in the Sezia Zone (Italian Western Alps). a record of the opening and closure of the Piedmont Ocean. Metamorphic Geol 9: 35-59

Li S, Wang S, Chen Y, Lui D, Qiu J, Zhou H,Zhang Z (1994) Excess argon in phengite from eclogite.Evidence from dating of eclogite by Sm-Nd, Rb-Sr and $^{40}Ar/^{39}Ar$ methods. Chem Geol(Isot Geosci Section) 112: 343-350

Maluski H, Monié P, Kienast JR, Rahmani A (1990) Locations of extraneous argon in granulitic-facies minerals. a paired microprobe-laser probe $^{40}Ar/^{39}Ar$ analysis. Chem Geol (Isot Geosci Section) 80: 193-217

Monié P (1985) La méthode $^{40}Ar/^{39}Ar$ appliquée au métamorphisme alpin dans le massif du Mont Rose (Alpes occidentales) Chronologie détaillée depuis 110 Ma. Eclogae Geol Helv 3: 487-516

Monié P, Philippot P (1989) Mise en évidence de l'âge éocène moyen du métamorphisme de haute pression dans la nappe ophiolitique du Monviso (Alpes occidentales) par la méthode $^{40}Ar/^{39}Ar$. CR Acad Sci, Paris 309: 245-251

Monié P, and Chopin C (1991) $^{40}Ar/^{39}Ar$ dating in a coesite-bearing eclogites and related units, Dora Maira massif, Western Alps. Eur J Mineral 3: 239-262

Paquette JL, Chopin C, Peucat JJ (1989) U-Pb zircon, Rb-Sr and Sm-Nd geochronology of high- to very-high-pressure meta-acidic rocks from the Western Alps. Contr Miner Petrol 101: 280-289

Roddick JC, Cliff RA, Rex DC (1980) The evolution of excess argon in alpine biotites. Earth Planet Sci Lett 48: 185-208

Scaillet S, Féraud G, Lagabrielle Y, Ballèvre M, Ruffet, G (1990) $^{40}Ar/^{39}Ar$ laser probe dating from the Dora Maira nappe of the Western Alps, Italy. Geology 18: 741-744

Scaillet S, Féraud G, Ballevre M, Amouric M (1992) Mg/Fe and [(Mg/Fe)Si-Al2] compositional control on argon behaviour in high pressure white micas. a $^{40}Ar/^{39}Ar$ continuous laser probe study from the Dora Maira nappe of the internal western Alps, Italy. Geochim Cosmochim Acta 56: 2851-2872

Schermer ER, Lux DR, Burchfiel BC (1990) Temperature-time history of subducted continental crust, Mount Olympus region, Greece. Tectonics 5: 1165-1195

Schertl HP, Schreyer W, Chopin C(1991) The pyrope-coesite rocks and their country rocks at Parigi, Dora Maira Massif, Western Alps. detailed petrography, mineral chemistry and P-T path. Contrib Miner Petrol 108: 1-21

Thoni M, Jagoutz E (1993) Isotopic constraints for eo-alpine high pressure metamorphism in the austroalpine nappes of the eastern Alps. bearing on alpine orogenesis. Bull Suisse Mineral Petrol 73,vol 2: 177-189

Tilton GR, Schreyer W, Schertl HP (1989) Pb-Sr-Nd isotopic behaviour of deeply subducted crustal rock from the Dora Maira massif, Western Alps, Italy. Geochim Cosmochim Acta 53: 1391-1400

Tilton GR, Schreyer W, Schertl HP(1991) Pb-Sr-Nd isotopic behaviour of deeply subducted crustal rock from the Dora Maira massif, Western Alps, Italy II. what is the age of the ultrahigh pressure metamorphism ?. Contrib Miner Petrol 108: 22-33

Vialette Y, Vialon P (1964) Etude géochronologique de queqlues micas des formations du massif Dora Maira (Alpes Cottiennes piémontaises). Ann Fac Sc Clermont-Ferrand Et Géochron I: 91-99

Vialon P (1966) Etude géologique du massif cristallin Dora maira, Alpes cottiennes internes, Italie. Thèse d'Etat, Université de Grenoble

Vidal Ph, Hunziker JC(1985) Systematics and problems in isotope work on eclogites. Chemical Geol 52: 129-141

Tables Captions.

Table 1: Microprobe analysis of phengite, biotite and feldspars. Typical analysis are shown with an average analysis. Numbers on analyses permit correlation of microprobe and argon laser analyses on fig 3. Note that analyses of pure minerals were hard to obtain because of intimate mixing with retrogressive biotite (phengite2 and 3 for example, or biotite 21). Structural formulae were calculated assuming 22 oxygen atoms and 2 H_2O molecules for micas, 24 oxygen atoms for garnets, and 8 oxygen atoms for feldspars. End member compositions of garnets are as follows. Al: almandine, Py: pyrope, Sp: spessartine, Gr: grossular. Fe^{2+}/Fe^{3+} for garnets have been calculated using Fe^{3+}= 4-(Al + Ti + Cr). $FM = \frac{Fe^{2+} + Mn}{Fe^{2+} + Mn + Mg}$

Table 2: $^{40}Ar/^{39}Ar$ data for quartz, micas and feldspars. Size of the laser pits and number of rasters (shown as #hits) are shown. Each raster ablates a depth of approximately 5µm. The mineralogy is given when it could be easily distinguished optically or when microprobe was performed at the same location. Otherwise a question mark is shown with the probable mineralogy. Measured signals (in moles) of each isotope are shown, with their errors. Note that due to very low quantitites of gas extracted the error on ^{36}Ar is taken to be 20% of the signal. In fact individual error on regression during each run might be higher but internal reproducibility on several analysis at the same location shows that 20% reflect the real error. (Data upon request from the authors). Consequently errors on $^{40}Ar/^{36}Ar$, $^{40}Ar^*/^{39}Ar$ (with atmospheric correction on ^{40}Ar) and age are calculated with that 20% error on ^{36}Ar. $^{40}Ar/^{39}Ar$ (with uncorrected ^{40}Ar) is given to compare, at similar ^{36}Ar values, the increase in ^{40}Ar content, which we interpret as excess argon. All data were corrected for mass spectrometer discrimination and irradiation interferences.

Figure captions.

Figure 1 (a). Sketch map of Dora Maira massif in the western Alps tectonic framework: 1: Briançonnais zone; 2: Schistes lustrés nappe; 3: internal crystalline massifs of Dora Maira (HP units) and Gran Paradiso (undifferentiated) ; 4: Austroalpine and Southalpine zones. Frame shows location of detailed map in figure 1b.

(b). Simplified map of southern Dora Maira with Brossasco-Isasca HP unit (from Henry et al., 1993, modified). The different basement eclogitic units are separated by major tectonic contacts. 1: Sanfront-Pinerolo unit of blue-schists and gneiss; Unit I: high temperature HP eclogitic unit composed of: 2: Parigi fine grain and augen gneisses with coesite-pyrope bearing lenses; 3: Isasca series (gneiss, metapelite marbles and metabasite); 4: orthogneissic mylonite; 5: intrusive Hercynian Brossasco metagranite. Unit II: cold HP unit undifferentiated. B locates Brossasco village, and the star locates the sampling area.

Figure 2. Example of a UV pit in K-feldspar imaged with SEM technique. Note the pattern of ejecta within the pit caused by the beam rastering process and the sharpness of the pit boundaries allowing adjacent pits to be drilled with gaps of 10 µm or less.

Figure 3. (a) microphotograph of typical pits in the Ph-Gt-Bio-Qz polymetamorphic aggregates. A sketch of the photograph is shown below. Note that pits selectively etch Ph, retrogressive red Bio only, or both. $^{40}Ar/^{39}Ar$ ratios are shown in each pit, together with the numbers of corresponding microprobe analyses in brackets, which refer to Table 1.

(b) traverse in a Kfd zone, from a large Kfd(pit 1) to small granoblastic Ab crystals (pit 5). A sketch of the photograph is shown below. The Or and Ab content of each analysis is shown under each pit with the number of each corresponding microprobe analysis in brackets, which refers to Table 1. The total $^{40}Ar/^{39}Ar$ is shown above each pit. Note that the amount of excess argon sharply increases at the contact with the granoblastic Ab grains and corresponds perfectly with the mineralogical/chemical boundary.

Figure 4. Inverse isochron diagrams of the different minerals analysed. (Qz) quartz; (Kfd2) alkali feldspars in small granoblastic bands, together with albite; (Ph+Bio1) phengites and retrogressive red biotite; (Bio2) red biotite in shear bands; (Kfd1) large igneous alkali feldspars. Various $^{39}Ar/^{40}Ar$ intercepts ages are shown with dashed lines to the atmospheric argon intercept. The solid 40 Ma line is shown as a reference for following mixing calculations (see text). The data define a broad conical envelope which spans from high $^{40}Ar/^{36}Ar$ ratios in Qz and Ph to Bio and Kfd which show the lowest

ages. This range is interpreted as the result of radiogenic growth of a variable initial mixture of excess argon with an atmospheric component.

Figure 5. Simple modelling of the result of radiogenic growth of a variable initial mixture of excess argon with an atmospheric component. As an example, an initial mixing envelope has been chosen (dotted rectangle) and allowed to evolve with time. The horizontal side of the box allows for variations in initial K content (therefore varying $^{39}Ar/^{40}Ar$) and the vertical side allows for varying initial excess component (varying $^{36}Ar/^{40}Ar$). The results are shown for 40 Ma, 100 Ma, 200 Ma and 400 Ma after mixing. Some $^{36}Ar/^{40}Ar$ ratios are shown above the abscissa. If the ratio of the excess component is known (in this case $^{36}Ar/^{40}Ar$ of 0.0015) the correct age can be calculated (ages shown below the abscissa). However, correcting results assuming an atmospheric ratio will lead to older ages shown by the dotted lines (and associated ages) which represent regression lines for the middle of each envelope. The discrepancy between the real and the false age increases with the time elapsed since mixing, while the false regression becomes better because the envelope is tightening with time, leading to better artificial plateaus. It is clear also that almost any initial envelope will tighten to a smaller one in which various spurious linear trends can be drawn. Note that if mixing took place 40 Ma ago, various trends can be drawn in the resulting envelope leading to ages in the range 80-120 Ma.

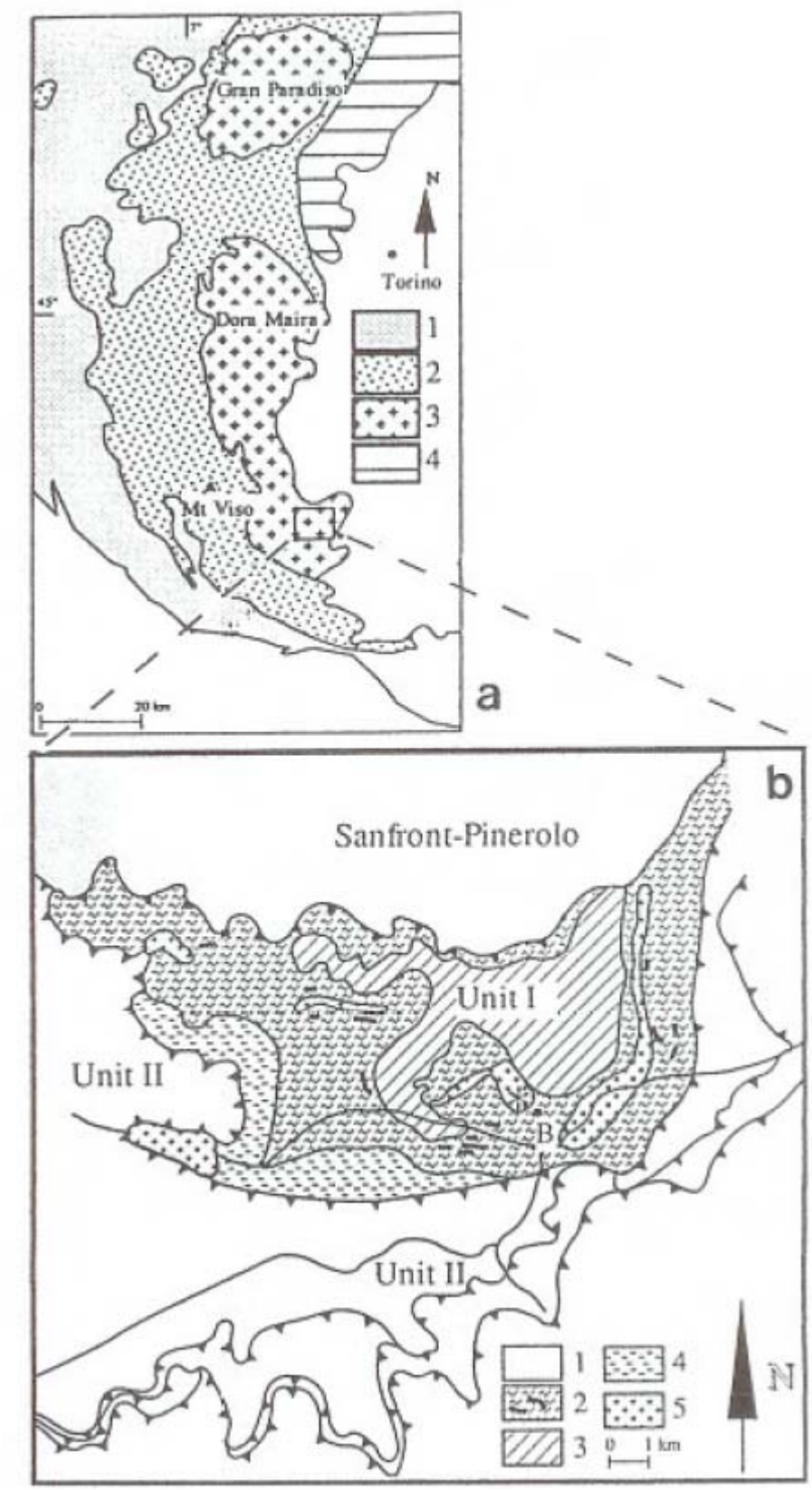
Gran Paradiso
Dora Maira
Mt Viso
Torino
N
1
2
3
4
a
b
Sanfront-Pinerolo
Unit I
Unit II
B
Unit II
1
2
3
4
5
0 1 km
N

Figure 1

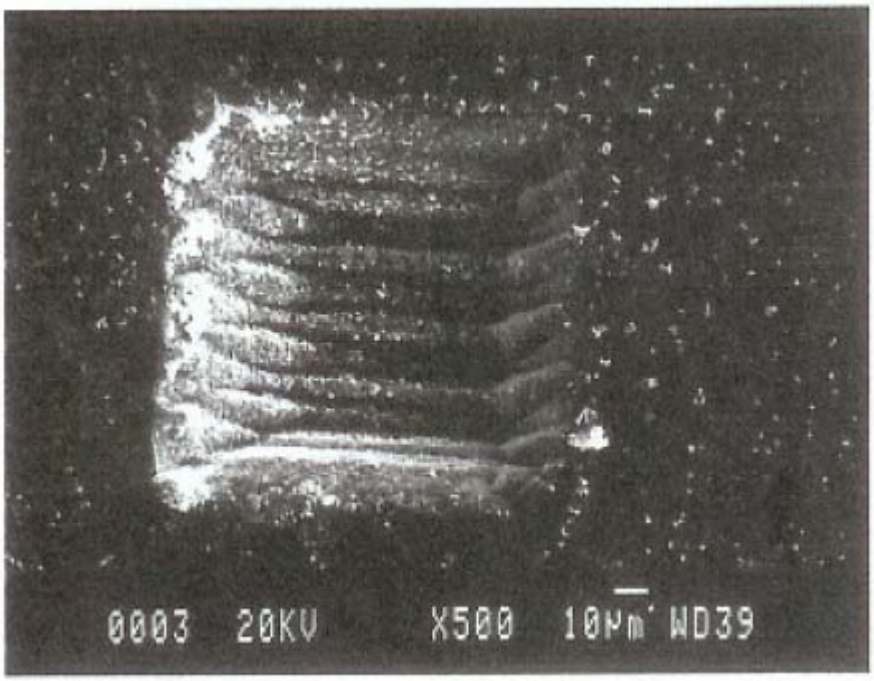

Figure 2

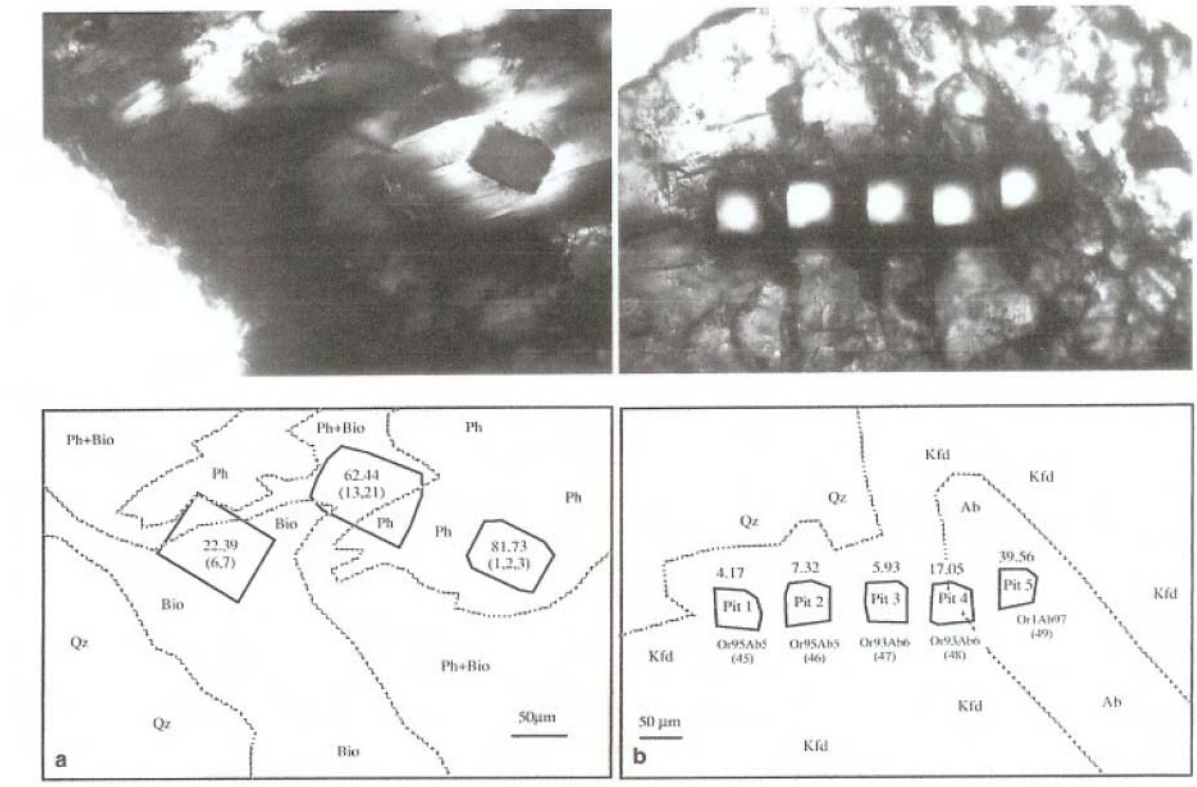
Ph+Bio
Ph+Bio
Ph
Ph
62.44
(13,21)
Ph
Bio
22.39
(6,7)
Ph
81.73
(1,2,3)
Bio
Qz
Ph+Bio
50µm
Qz
Bio
a
Kfd
Kfd
Qz
Qz
Ab
39.56
4.17
7.32
5.93
17.05
Pit 5
Pit 1
Pit 2
Pit 3
Pit 4
Kfd
Or1Ab97
(49)
Or95Ab5
(45)
Or95Ab5
(46)
Or93Ab6
(47)
Or93Ab6
(48)
Kfd
Kfd
Ab
50 µm
Kfd
b

Figure 3

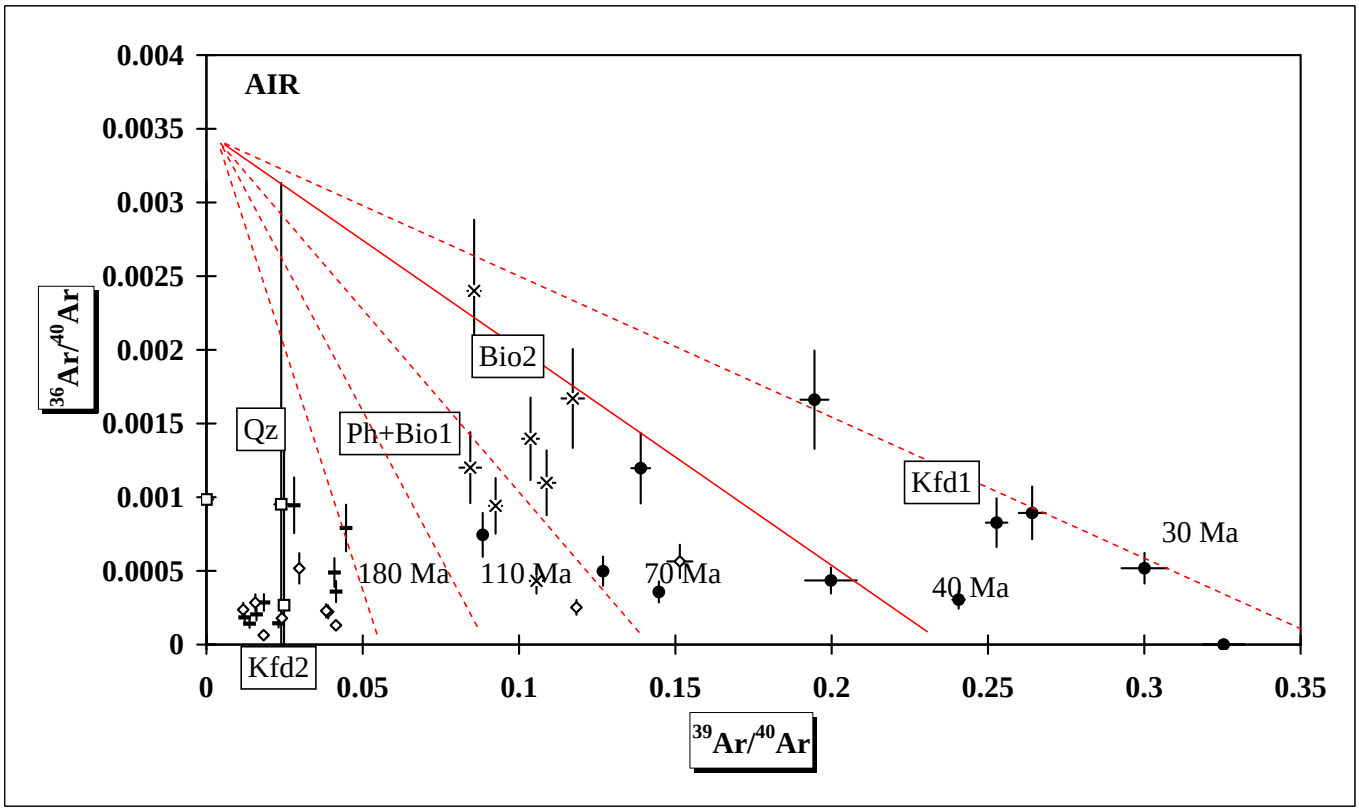

Figure 4, Arnaud and Kelley, 1995

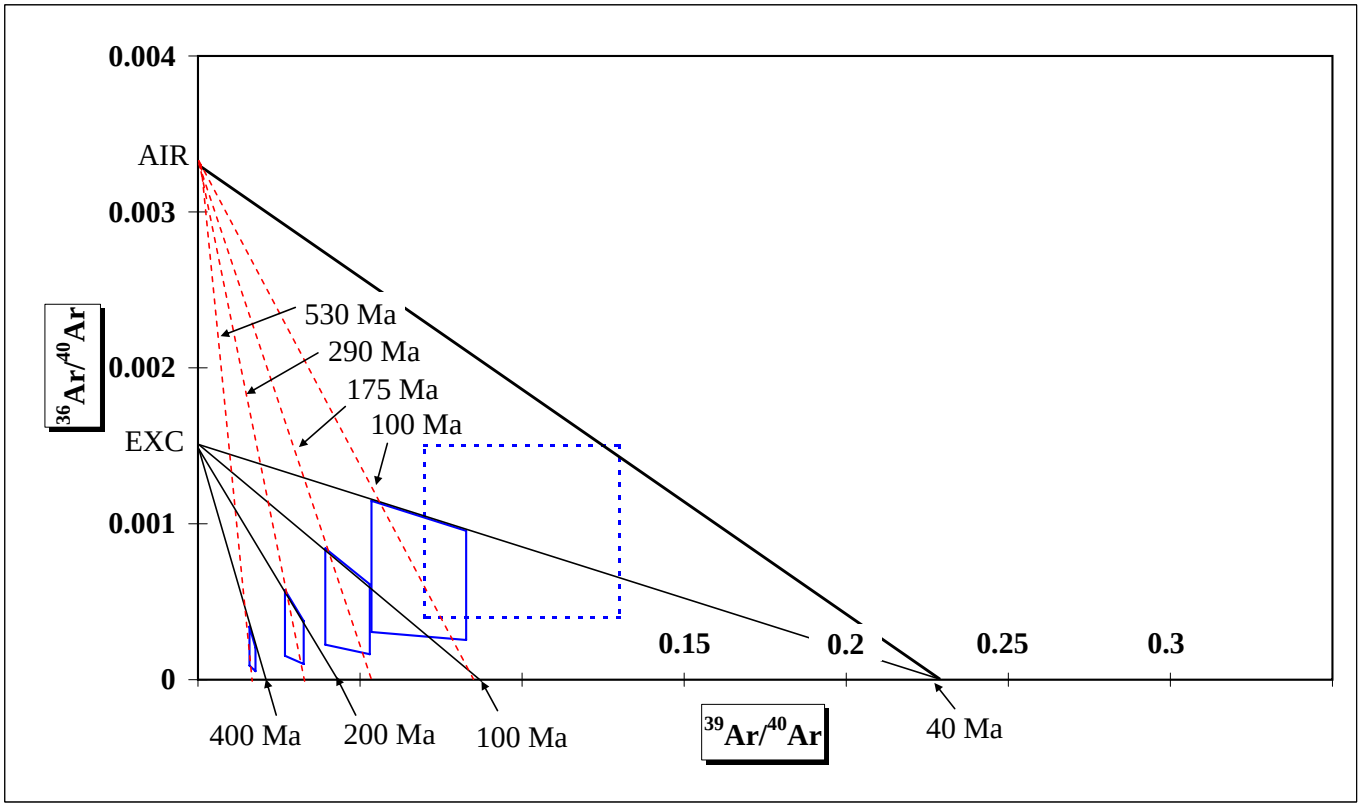

Figure 5, Arnaud and Kelley, 1994

Phengites	1	2	3	10	13	16	Ave
K20	10.92	9.07	9.37	10.46	11.12	9.57	10.09
CaO	0.01	0.14	0.06	0.06	0.00	0.01	0.05
TiO	1.86	1.75	2.30	1.29	1.43	1.58	1.70
FeO	3.99	4.27	3.83	3.59	3.77	3.87	3.89
MnO	0.03	0.04	0.05	0.02	0.12	0.00	0.04
Cr2O3	0.06	0.08	0.07	0.04	0.18	0.00	0.07
Na2O	0.15	0.48	0.20	0.27	0.16	0.15	0.24
SiO2	51.71	54.50	53.96	51.62	50.89	53.22	52.65
Al2O3	25.31	25.43	24.33	26.33	25.48	26.24	25.52
MgO	3.04	3.02	3.58	2.84	2.92	3.24	3.11
OH	4.52	4.66	4.61	4.52	4.47	4.62	4.57
tot	101.61	103.44	102.37	101.04	100.53	102.50	101.92
Structural Formula							
K	1.85	1.49	1.55	1.77	1.90	1.59	1.69
Ca	0.00	0.02	0.01	0.01	0.00	0.00	0.01
Ti	0.19	0.17	0.23	0.13	0.14	0.15	0.17
Fe total	0.44	0.46	0.42	0.40	0.42	0.42	0.43
Mn	0.00	0.00	0.01	0.00	0.01	0.00	0.01
Cr	0.01	0.01	0.01	0.00	0.02	0.00	0.01
Na	0.04	0.12	0.05	0.07	0.04	0.04	0.06
Si	6.85	7.00	7.01	6.84	6.82	6.91	6.91
Al	3.95	3.85	3.73	4.11	4.03	4.01	3.95
Mg	0.60	0.58	0.69	0.56	0.58	0.63	0.61
OH	2.00	2.00	2.00	2.00	2.00	2.00	2.00
tot	15.93	15.70	15.70	15.89	15.98	15.74	15.82

Table 1

Biotite	6	7	16	21	22	26	Ave
K20	9.46	9.63	9.93	8.72	8.93	9.18	9.31
CaO	0.03	0.00	0.06	0.05	0.08	0.04	0.04
TiO	1.76	1.72	0.58	2.79	2.01	2.00	1.81
FeO	24.18	23.66	19.82	20.20	21.90	20.69	21.74
MnO	0.38	0.36	0.29	0.19	0.33	0.18	0.29
Cr2O3	0.00	0.09	0.00	0.02	0.02	0.04	0.03
Na2O	0.29	0.03	0.23	0.02	0.26	0.38	0.20
SiO2	37.20	36.03	39.76	46.84	37.31	39.93	39.51
Al2O3	17.15	17.68	16.91	14.02	17.22	18.69	16.95
MgO	7.23	6.80	5.95	5.29	6.40	6.49	6.36
OH	3.95	3.88	3.88	4.17	3.87	4.07	3.97
tot	101.62	99.88	97.41	102.32	98.33	101.67	100.21
Structural Fomula							
K	1.83	1.90	1.95	1.60	1.76	1.72	1.79
Ca	0.01	0.00	0.01	0.01	0.01	0.01	0.01
Ti	0.20	0.20	0.07	0.30	0.23	0.22	0.20
Fe total	3.07	3.06	2.56	2.43	2.83	2.55	2.75
Mn	0.05	0.05	0.04	0.02	0.04	0.02	0.04
Cr	0.00	0.01	0.00	0.00	0.00	0.00	0.00
Na	0.08	0.01	0.07	0.01	0.08	0.11	0.06
Si	5.64	5.57	6.13	6.72	5.77	5.88	5.95
Al	3.07	3.22	3.07	2.37	3.14	3.24	3.02
Mg	1.63	1.56	1.37	1.13	1.47	1.42	1.43
OH	2.00	2.00	2.00	2.00	2.00	2.00	2.00
tot	17.58	17.57	17.27	16.59	17.35	17.19	17.26

Arnaud and Kelley, 1995

K-feldspar	12	14	44	45	46	47	48	50	51	Ave
K20	15.90	16.25	15.40	15.63	16.04	15.94	0.16	0.16	0.16	10.63
CaO	0.00	0.00	0.04	0.16	0.07	0.03	0.00	0.00	0.00	0.03
TiO	0.00	0.03	0.03	0.00	0.04	0.00	0.00	0.00	0.00	0.01
FeO	0.00	0.00	0.05	0.15	0.00	0.00	0.00	0.00	0.00	0.02
MnO	0.00	0.03	0.00	0.00	0.00	0.03	0.00	0.00	0.00	0.01
Cr2O3	0.00	0.01	0.03	0.00	0.00	0.00	0.00	0.00	0.00	0.00
Na2O	0.51	0.58	0.70	0.68	0.67	0.26	0.01	0.01	0.00	0.38
SiO2	62.57	63.01	63.27	62.36	63.29	63.02	0.62	0.63	0.63	42.16
Al2O3	18.28	18.55	18.18	17.99	18.12	17.91	0.18	0.18	0.18	12.17
MgO	0.04	0.01	0.01	0.02	0.04	0.01	0.00	0.00	0.00	0.01
tot	97.30	98.46	97.72	96.97	98.27	97.20	0.97	0.98	0.97	65.43
Struc. form										
K	0.96	0.94	0.93	0.96	0.98	0.93	0.95	0.96	0.97	0.95
Ca	0.00	0.00	0.00	0.00	0.00	0.00	0.01	0.00	0.00	0.00
Ti	0.00	0.00	0.00	0.00	0.00	0.00	0.00	0.00	0.00	0.00
Fe total	0.00	0.00	0.00	0.00	0.00	0.00	0.01	0.00	0.00	0.00
Mn	0.00	0.00	0.00	0.00	0.00	0.00	0.00	0.00	0.00	0.00
Cr	0.00	0.00	0.00	0.00	0.00	0.00	0.00	0.00	0.00	0.00
Na	0.05	0.07	0.06	0.05	0.05	0.06	0.06	0.06	0.02	0.05
Si	3.00	3.00	3.00	2.98	2.97	2.99	2.98	2.98	3.00	2.99
Al	1.00	1.00	1.00	1.03	1.03	1.01	1.01	1.01	1.00	1.01
Mg	0.00	0.00	0.00	0.00	0.00	0.00	0.00	0.00	0.00	0.00
tot	5.01	5.01	5.00	5.02	5.03	5.00	5.02	5.02	5.00	5.01
Ab	0.05	0.07	0.06	0.05	0.05	0.06	0.06	0.06	0.02	0.05
Or	0.95	0.93	0.94	0.95	0.95	0.93	0.93	0.94	0.97	0.94
An	0.00	0.00	0.00	0.00	0.00	0.00	0.01	0.00	0.00	0.00

	15	52	49	31	Ave
K20	0.17	0.18	0.36	0.28	0.25
CaO	0.36	0.29	0.83	1.09	0.64
TiO	0.03	0.00	0.05	0.00	0.02
FeO	0.26	0.01	0.02	0.13	0.11
MnO	0.02	0.00	0.03	0.00	0.01
Cr2O3	0.00	0.07	0.00	0.03	0.03
Na2O	11.08	10.73	10.52	10.30	10.66
SiO2	67.17	67.14	66.18	66.89	66.85
Al2O3	19.68	19.26	19.53	19.99	19.62
MgO	0.18	0.05	0.00	0.04	0.07
tot	98.97	97.74	97.51	98.76	98.25
Struc. form					
K	0.01	0.01	0.02	0.02	0.01
Ca	0.02	0.01	0.04	0.05	0.03
Ti	0.00	0.00	0.00	0.00	0.00
Fe total	0.01	0.00	0.00	0.00	0.00
Mn	0.00	0.00	0.00	0.00	0.00
Cr	0.00	0.00	0.00	0.00	0.00
Na	0.95	0.93	0.91	0.88	0.92
Si	2.97	3.00	2.97	2.96	2.97
Al	1.03	1.01	1.03	1.04	1.03
Mg	0.01	0.00	0.00	0.00	0.00
tot	5.00	4.97	4.98	4.97	4.98
Ab	0.97	0.97	0.94	0.93	0.95
Or	0.01	0.01	0.02	0.02	0.01
An	0.02	0.01	0.04	0.05	0.03

Garnets	9	11	65	69	Ave
K20	0.19	0.11	0.03	0.03	0.09
CaO	14.84	11.38	17.04	13.94	14.30
TiO	0.04	0.03	0.13	0.12	0.08
Fe2+	24.15	27.08	22.91	25.15	24.82
Fe3+	0.00	0.00	0.15	0.06	0.05
MnO	0.00	0.69	1.31	1.21	0.80
Cr2O3	0.06	0.00	0.04	0.00	0.03
Na2O	0.00	0.03	0.00	0.03	0.02
SiO2	38.33	38.52	38.31	38.09	38.31
Al2O3	22.07	21.78	21.76	21.57	21.80
MgO	1.16	1.79	0.52	0.99	1.12
tot	100.84	101.42	102.20	101.19	101.41
Struc. form					
K	0.04	0.02	0.01	0.01	0.02
Ca	2.48	1.90	2.83	2.34	2.39
Ti	0.00	0.00	0.02	0.01	0.01
Fe2+	3.15	3.53	2.97	3.30	3.24
Fe3+	0.00	0.00	0.02	0.01	0.01
Mn	0.00	0.09	0.17	0.16	0.11
Cr	0.01	0.00	0.01	0.00	0.00
Na	0.00	0.01	0.00	0.01	0.00
Si	5.98	6.01	5.94	5.97	5.98
Al	4.06	4.01	3.97	3.99	4.01
Mg	0.27	0.42	0.12	0.23	0.26
tot	15.99	16.00	16.05	16.02	16.02
FM	0.92	0.90	0.96	0.94	0.93
Al	0.53	0.59	0.49	0.55	0.54
Py	0.05	0.07	0.02	0.04	0.04
Sp	0.00	0.02	0.03	0.03	0.02
Gr	0.42	0.32	0.46	0.38	0.39

Arnaud and Kelley, 1995 Table 1, cont.

Quartz

Sample	Pit size (µm)	#hits	40Ar/36Ar	±	40Ar/39Ar	±
abw2	100X100	6	1015.79	462.53	9.72E+07	462.54
abx103	100X100	6	63.39	114.82	50.42	114.37
aby16	100X100	6	1050.29	458.49	41.79	452.54
aby23	70X70	12	3741.88	807.69	40.26	793.45

Table 2

Arnaud and Kelley, 1995

Micas

Sample	Pit size (µm)	#hits	Mineralogy	40Ar/36Ar	±	40Ar/39Ar	±	40Ar*/39Ar	±	Age (Ma)	±
abw123	50X50	15	Phengite	7054.98	1411.04	72.54	1.01	69.50	1.15	565.35	10.79
abx92	70X80	10	Phengite	5422.14	1084.47	81.73	1.64	77.27	1.78	614.33	14.25
abx94	100X100	10	Biotite1	2044.23	408.98	24.43	0.46	20.90	0.81	187.81	7.41
abx96	100X100	10	Phengite/Biotite1	4883.40	976.93	62.44	1.98	58.67	2.01	484.40	15.82
abx98	100X100	10	Biotite1	1264.23	253.14	22.39	0.44	17.16	1.11	155.59	9.86
abx101	50X50	10	Phengite/Biotite1	3497.90	699.62	54.38	1.75	49.79	1.85	418.95	14.94
abx105	100X100	6	Biotite1	1058.00	211.72	35.64	0.63	25.69	2.05	228.24	17.38
abx107	100X100	5	Biotite1	2782.81	557.07	24.12	0.49	21.56	0.68	193.44	6.36
abx109	100X100	7	Phengite/Biotite1	6925.95	1385.46	43.32	0.43	41.48	0.56	355.41	6.42
aby2	200X50	7	Biotite2	911.13	183.03	9.19	0.24	6.21	0.63	57.87	5.84
aby4	70X70	8	Biotite2	416.61	83.71	11.68	0.29	3.39	1.67	31.87	15.57
aby7	100X100	6	Biotite2	338.77	73.60	13.19	2.28	1.68	2.57	15.89	24.15
aby9	200X25	7	Biotite2	598.82	120.32	8.53	0.26	4.32	0.86	40.48	8.03
aby11	50X50	10	Biotite2	374.61	77.88	7.68	0.83	1.62	1.30	15.29	12.17
aby14	200X25	7	Biotite2	667.96	134.06	11.13	0.49	6.21	1.03	57.86	9.51
aby19	70X70	12	Biotite2	2312.49	463.48	9.47	0.20	8.26	0.30	76.59	2.97
aby21	70X70	12	Biotite2	832.84	167.18	11.85	0.49	7.64	0.91	70.99	8.36
aby25	70X70	12	Biotite2	715.92	143.39	9.65	0.25	5.66	0.81	52.87	7.53
aby27	70X70	12	Biotite2	1939.20	388.74	10.96	0.31	9.29	0.43	85.92	4.08
aby29	70X70	12	Biotite2	1062.00	212.79	10.81	0.25	7.80	0.63	72.43	5.86

Feldspars

Sample	Pit size (µm)	#hits	Mineralogy	40Ar/36Ar	±	40Ar/39Ar	±	40Ar*/39Ar	±	Age (Ma)	±
aby32	100X100	6	Albite ?	4496.19	899.76	25.69	0.79	24.00	0.82	214.12	7.49
aby34	100X100	6	Albite ?	7635.05	1527.22	24.13	0.45	23.20	0.47	207.36	4.92
aby36	50X50	6	Albite ?	no 36Ar	-	13.05	0.32	13.05	0.32	119.59	3.31
aby38	100X100	6	Albite ?	4223.30	844.69	84.97	0.62	79.03	1.32	626.11	11.77
aby40	100X100	6	Albite ?	4367.99	873.72	26.10	0.25	24.33	0.43	216.90	4.67
aby42	100X100	6	K-feldspar 2	no 36Ar	-	6.47	0.16	6.47	0.16	60.24	1.72
aby44	100X100	6	Albite ?	5586.65	1117.51	41.42	0.86	39.23	0.93	337.88	8.56
aby46	100X100	6	Albite ?	15671.32	3134.55	54.64	0.75	53.61	0.76	447.44	8.09
aby49	100X100	6	Albite ?	no 36Ar	-	19.10	0.59	19.10	0.59	172.36	5.63
aby51	100X100	6	Albite ?	3515.05	703.02	63.92	0.72	58.55	1.26	483.54	11.04
aby53	100X100	6	K-feldspar 2	3961.76	792.50	8.45	0.09	7.82	0.15	72.58	1.73
aby55	100X100	6	Albite ?	1933.60	386.79	33.67	0.46	28.52	1.10	251.73	9.72
aby57	50X50	6	K-feldspar 2	334.70	69.01	3.14	0.18	0.37	0.58	3.48	5.45
aby59	50X50	6	Albite ?	no 36Ar	-	11.67	0.23	11.67	0.23	107.26	2.57
aby61	100X100	6	K-feldspar 2	1772.02	355.08	6.60	0.18	5.50	0.27	51.38	2.58
aby66	100X100	6	K-feldspar 2	389.96	78.97	3.17	0.11	0.77	0.49	7.25	4.63
aby68	50X50	6	K-feldspar 2	no 36Ar	-	4.17	0.16	4.17	0.16	39.03	1.63
aby71	50X50	6	K-feldspar 2	316.49	63.59	7.32	0.21	0.49	1.37	4.59	12.98
aby73	50X50	6	K-feldspar 2	345.36	70.22	5.93	0.30	0.86	1.04	8.09	9.79
aby75	50X50	6	Albite	no 36Ar	-	17.05	0.41	17.05	0.41	154.67	4.19
aby77	50X50	6	Albite	472.57	94.69	39.56	3.03	14.82	5.10	135.22	44.83
abv66	100X100	10	K-feldspar 1	2008.30	402.20	7.88	0.11	6.72	0.25	63.86	2.53
abw4	100X100	10	K-feldspar 1	601.81	120.85	5.14	0.12	2.62	0.51	25.13	4.92
abw6	100X100	10	K-feldspar 1	2298.18	465.30	5.01	0.21	4.36	0.23	41.70	2.30
abw8	200X200	10	K-feldspar 1	835.29	167.34	7.20	0.16	4.65	0.52	44.43	4.98
aby81	100X100	6	K-feldspar 1	no 36Ar	-	5.34	0.07	5.62	0.09	53.54	1.14
aby83	50X50	10	K-feldspar 1	1930.24	388.25	3.33	0.08	2.82	0.13	27.09	1.29
aby85	50X50	10	K-feldspar 1	no 36Ar	-	3.07	0.06	3.07	0.06	29.48	0.73
aby87	100X100	6	K-feldspar 1	1119.22	224.30	3.79	0.06	2.79	0.21	26.75	2.01
aby90	100X100	6	K-feldspar 1	3280.78	656.43	4.16	0.03	3.78	0.08	36.20	0.93
aby92	100X100	6	K-feldspar 1	2799.37	560.29	6.91	0.06	6.18	0.16	58.80	1.70
abz3	100X100	6	K-feldspar 1	no 36Ar	-	3.27	0.06	3.35	0.06	32.11	0.76
abz5	100X100	6	K-feldspar 1	1208.43	241.93	3.96	0.05	2.99	0.20	28.67	1.94
abz7	100X100	6	K-feldspar 1	1343.33	268.99	11.32	0.18	8.83	0.52	83.39	4.97
abz9	100X100	6	K-feldspar 1	309.07	63.24	6.70	0.37	0.29	1.31	2.84	12.68